Tank Testing of a Windfoil Hydrofoil with Free Surface Effects

Patrick Bot, Frédéric Hauville, Patrick Ploé, Jules Longuet

Patrick Bot, Frédéric Hauville, Patrick Ploé, Jules Longuet. Tank Testing of a Windfoil Hydrofoil with Free Surface Effects. Journal of Sailing Technology, 2025, 10 (01), pp.191-205. ⟨10.5957/jst/2025.10.1.191⟩. ⟨hal-05497999⟩

Journal of Sailing Technology 2025, volume 10, issue 1, pp. 191-205.
The Society of Naval Architects and Marine Engineers.

Tank Testing of a Windfoil Hydrofoil with Free Surface Effects

Patrick Bot
Arts et Métiers Institute of Technology, IRENav, France, patrick.bot@ecole-navale.fr

Frédéric Hauville
Arts et Métiers Institute of Technology, IRENav, France.

Patrick Ploé
VPLP Design, France.

Jules Longuet
Arts et Métiers Institute of Technology, IRENav, France.

Manuscript received March 20, 2025; revision received June 03, 2025; accepted July 13, 2025.

Abstract. Hydrofoils used on many water crafts and boats, operate in close proximity to the free surface. While the behavior of wings in a single-fluid medium is well known, the effects of the free surface on hydrofoils are not precisely known. The high computational cost of CFD simulations with the air-water interface makes them difficult to be used to build a full hydrodynamic surrogate model with many input parameters, as needed for a Velocity Prediction Program (VPP). For a small hydrofoil, it is possible to test the full-scale foil in a towing tank and measure the hydrodynamic forces. This work presents a test campaign of the main lifting wing of the Olympic Class windfoil (IQFoil) hydrofoil in the towing tank of Centrale Nantes. The measurements carried out in different configurations of immersion, heel and trim, allow for exploring the operation of the hydrofoil and the impact of the proximity of the free surface on its performances. It is shown that the lift force and slope with angle of attack are reduced when approaching the free surface and that the variations of drag are dominated by the induced drag. When the wing pierces the free surface, ventilation may occur resulting in a sharp drop in lift. These experimental results can be used as a validation benchmark for numerical simulations and are useful to build the hydrodynamic force model intended to supply a VPP.

Keywords: hydrofoil; windfoil; IQFoil; free surface; towing tank; VPP.

NOMENCLATURE

α	Angle of attack of the wing [° or rad]
α_0	Zero-lift angle of attack [° or rad]
$A_R = b^2/S$	Aspect Ratio [-]
$A_{Reff} = eA_R$	Effective aspect ratio [-]
$b = 0.9\,\mathrm{m}$	Wing span [m]
$c = 0.125\,\mathrm{m}$	Chord length of the wing in the center [m]
$C_D = D/0.5\rho U^2 S$	Drag force coefficient [-]
$C_{D_{min}}$	Minimum drag coefficient according to α [-]
$C_L = L/0.5\rho U^2 S$	Lift force coefficient [-]
$C_{L_{md}}$	Lift coefficient at minimum drag [-]
D	Drag force in the direction of the flow [N]
e	Oswald coefficient [-]

$Fr = U/\sqrt{gc}$	Chord-based Froude number [-]
$g = 9.81\,\mathrm{m\,s^{-2}}$	Acceleration of gravity [m s^{-2}]
h	Immersion depth of the center of the wing chord in the center [m]
L	Lift force in the direction normal to the flow and wing span [N]
$S = 0.08\,\mathrm{m^2}$	Projected wing surface area [m^2]
U	Carriage velocity [m s^{-1}]

ρ	Fluid density [kg m^{-3}]
θ	Heel angle [°]

AoA	Angle of Attack
CFD	Computational Fluid Dynamics
IQFoil	Olympic Class windfoil
VPP	Velocity Prediction Program

1 INTRODUCTION

Hydrofoils are now used on many foiling boats and crafts. They move in close proximity to the free surface or even pierce it, so it is important to assess the impact of the free surface on the hydrodynamic forces developed by these foils. Various numerical methods have been developed to take into account the proximity of the air-water interface. These methods include the use of a simple (anti)symmetry plane or a linearized Neumann-Kelvin condition in potential fluid solvers (Perali et al., 2022; Perali et al., 2024; Nicolas et al., 2023), and the bi-fluid resolution with interface tracking in RANS solvers (Pernod et al., 2023; Jego, 2022). These latter methods are generally considered as reference, but their high computational cost often constitutes a barrier to their large-scale use, as is necessary, for example, to build a hydrodynamic force substitution model intended to feed a Velocity Prediction Program (VPP) with many input parameters. Moreover, these so-called high-fidelity methods would benefit from being compared to experimental measurements to validate and refine the numerical parameters of the models. Experimental data on hydrofoils close to the free surface under realistic conditions are rare in the literature (Binns et al., 2008; Daskovsky, 2000), in particular for high Froude numbers. However, there is a real need for more experimental work to measure the variations in forces developed by a hydrofoil as a function of immersion.

The IQFoil is the Olympic Class for windfoiling (Fig. 1) since the 2024 Games. The foil package is made of the main lifting front wing and the rear stabilizer linked by the fuselage, which is connected to the board by the foil mast or shaft. A few recent works have built Velocity Prediction Programs of this class of windfoil to investigate performances and the influence of different parameters (Hochhausen et al., 2024; Hou et al., 2024a). The aerodynamics of the IQFoil sail was studied experimentally by Mok et al. (2023) and numerically by Hou et al. (2024b). For the hydrodynamic force models used in their VPP, Hochhausen et al. (2024) resolve the flow around the foil package with the classical extended vortex lattice model Athena Vortex Lattice (AVL) developed by Mark Drela (Drela and Youngren, 2011), and Hou et al. (2024a) use force coefficients measured on the foil in a wind tunnel. Furthermore, de la Hougue et al. (2022) performed a fluid structure investigation to study the influence of the shaft stiffness on windfoil performance. Finally, de la Hougue et al. (2021) studied six IQFoil wings with slightly different geometries with an XFoil-coupled panel method to relate their hydrodynamic performances to the feedback from high-level sailors who tested the different wings. However, to the best of our knowledge, no experimental results are reported on this kind of hydrofoil in realistic conditions.

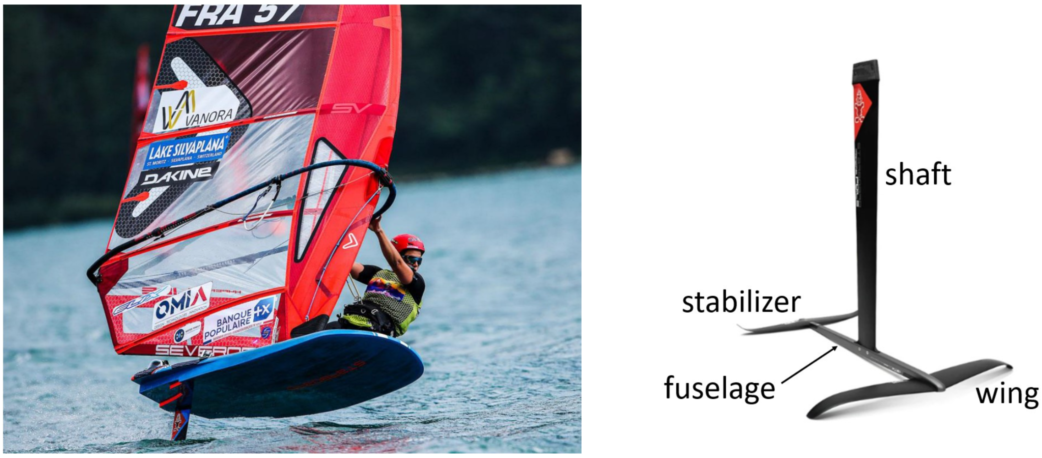

Figure 1. Olympic Class windfoil: IQFoil. Note the curved span of the main wing and the drooped tips.

The relative velocity of the foil in a flow causes a pressure difference between the lower and upper surfaces of the wing. This pressure difference generates lift and drag induced by this lift. Another part of the drag is due to viscous forces exerted by the water on the moving wing. The flow around a foil is further influenced by the presence of the free surface. Thanks to tank testing and theoretical developments, Wadlin et al. (1955) showed that at shallow depth, the effects of the water surface must be taken into account. They developed methods for predicting the lift and drag of hydrofoils as they approach the water surface and found reasonable agreement with experiments. Wadlin and Christopher (1958) derived a method to calculate the lift coefficient for rectangular lifting surfaces at finite depth, including zero depth in planning condition. The method is also applicable to hydrofoils with dihedral up to 30°, by considering the varying influence of depth over the span. Parkin et al. (1955) evidenced two distinct regimes depending on the chord-based Froude number, and Hough and Moran (1969) highlighted the Froude number effects. Among various works about ventilation, Harwood et al. (2016) performed an experimental investigation and identified the stability domains of fully wetted, fully ventilated and partially ventilated flow regimes. Finally, Harwood et al. (2019) and Harwood et al. (2020) also considered the fluid structure interaction of ventilated foils. The following list presents the four major effects of the free surface that can be expected (Faltinsen, 2005; Hough and Moran, 1969):

- The pressure field: The pressure field is affected by the proximity of the free surface. The flow over the foil is limited by the upper surface and by the free surface, thus modifying the suction. This induces a loss of lift for Froude numbers greater than 1.
- The wave field: The pressure field around the foil will cause a deformation of the free surface and this deformation will generate a wave drag, which depends on the immersion, the wing angle of attack, the heel angle and the Froude number.
- The spray and roll-up: In the case where the wing pierces the free surface, projections occur and cause an additional drag called spray drag; water also runs upwards on the emerging body and this so-called roll-up generates an extra drag.
- Ventilation: The pressure on the faces of the wing can reach a value lower than atmospheric pressure in cases where the foil is close to the surface. This can result in suction forming an air pocket covering part of the wing suction side. This ventilation causes a drop in lift and an increase in drag.

This work presents an experimental campaign where a hydrofoil of the current Olympic class windfoil, namely the IQFoil, is tested in a towing tank at high Froude number, to measure the actual hydrodynamic forces generated and how they are affected by the free surface. The experimental system is described in section 2, section 3 presents the results on measured lift and drag coefficients, section 4 analyzes the measured data to propose a global characterization of forces variations, and conclusions are given in section 5.

2 EXPERIMENTAL SETUP

The experiments were carried out in the towing tank of the LHEEA laboratory of Centrale Nantes, France. The tank has a length of 140 m, a width of 5 m and a constant depth of 3 m. The towing carriage has a theoretical maximum speed of 8 m s^{-1}. A Stewart platform, type MISTRAL from SYMETRIE, is fixed upside down on the frame "Monte & Baisse" (M&B) of the carriage (yellow frame in Fig. 2). The Stewart platform has two plates. The base plate is fixed to the M&B and the movable plate is connected by six electric linear actuators to the base plate. The plates and actuators are connected by Cardan joints that allow the movable plate to be moved in the six degrees of freedom. The Stewart platform is controlled by a PC and is used to position the movable plate in the target position and attitude. Only static tests have been performed without foil movement nor swell. The M&B frame allows the increase of the stroke along the vertical Z axis of the carriage. A 6-component force balance is fixed on the movable plate of the Stewart platform (cylindrical part under the hexapod plate in Fig. 2) and the foil mast (or shaft) is fixed under the balance by clamping. The test rig was designed with the force balance below the orientation system (Stewart platform) to ensure that it is in the same coordinate system as the foil. As no yaw angle is considered in the present work, the main force component is expected to be in the direction orthogonal to the wing plane, mostly along the direction of the shaft, then always in the same axis as the sensor. Hence, it is chosen to define the lift force in the direction orthogonal to the wingspan and to the onset flow direction (i.e. in the plane of the shaft). Then, the vertical and side force components are simply obtained by projecting this lift force with the heel angle.

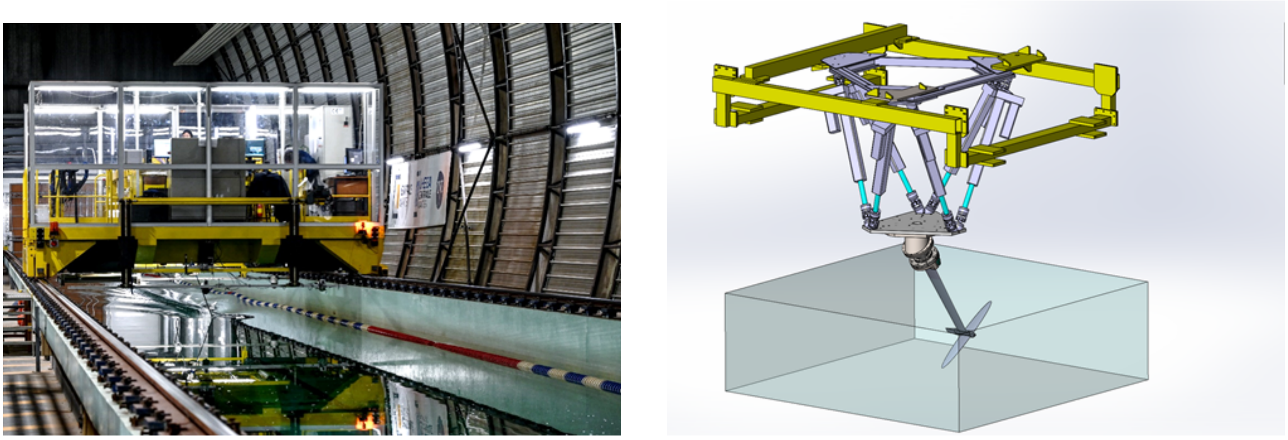

Figure 2. Experimental setup.

It was not possible to test the complete foil package of the IQFoil because the wing-stabilizer combination generates a high pitching moment that exceeds the force sensor capacity. As such, only the main lifting wing is measured. The same shaft is used to hold the wing via a custom-made connecting piece that holds the wing below the shaft and the force sensor. The top of the shaft is clamped to the bottom of the 6-degree-of-freedom force sensor, which was designed and built specifically for this application.

The orientation and immersion of the foil are modified by combining the movements of the Stewart platform and the M&B - Table 1. A heeling wedge of 35° was also manufactured and set between the platform and the force sensor in order to be able to reach larger heeling angles. The values ”Stewart” specified in Table 1 are only valid for each degree of freedom taken separately and are limited in the case of combinations.

Table 1. Possible positions and attitudes with the experimental system.

	Stewart	Monte & Baisse	Heeling wedge	Total
TX (mm)	± 460	0	0	± 460
TY (mm)	± 460	0	0	± 460
TZ (mm)	± 400	±700	0	± 1100
RX (°)	± 30	0	+35	-30 to +65
RY (°)	± 30	± 5	0	± 35
RZ (°)	± 40	0	0	± 40

The IQFoil wing has been tested at a towing velocity $U = 7\,\mathrm{m\,s^{-1}}$ for different values of the parameters: immersion depth-to-chord ratio $h/c \in [0.125; 6]$, heel angle $\theta \in [0°; 60°]$, angle of attack $\alpha \in [-4°; 6°]$. Because of geometrical and experimental constraints, not all combinations could be tested. A total of 192 runs were measured during two testing campaigns. During the first campaign in April-May 2023, a custom-made 6-component force sensor, specially designed for this experiment and manufactured by the company Sixaxes (model FX2.6 No. 1287), is used. This strain gauge sensor can measure the three force components and the three moment components, with an expanded uncertainty (k=2) of less than 0.4% of the measurement range, including the interchannels. The test body is composed of 4 elastic beams in stainless steel with a high elastic limit, and equipped with ”semis” gauges in an optimized number in order to maximize each measurement and minimize interchannels. Unfortunately, this tailor-made sensor was damaged during another project and could not be repaired. Then, for the second campaign in January-February 2024, another sensor already available is used (HBK-MCS10BG2-025). The latter leads to limits in the loading in M_x and even if the accuracy of the sensor is 0.2% of the measuring range, the force ranges of this second sensor being clearly higher, the absolute accuracy is lower (Table 2). Nevertheless, the repeatability of the measurements between both campaigns was tested and deemed acceptable.

Table 2. Measurement ranges for each sensor used in the tests.

	Sixaxes FX2.6 N° 1287	HBK-MCS10BG2-025
F_X (N)	± 400	± 5000
F_Y (N)	± 2000	± 5000
F_Z (N)	± 2000	± 25000
M_X (N.m)	± 1200	± 350
M_Y (N.m)	± 240	± 350
M_Z (N.m)	± 100	± 250

The IQFoil main wing that is studied here has a projected surface $S = 0.08\,\mathrm{m}^2$, a wing span $b = 0.9\,\mathrm{m}$ and a maximum chord length in the center $c = 0.125\,\mathrm{m}$. The geometric aspect ratio is $A_R = b^2/S = 10.125$. The profile of the section is cambered and close to the H105 section with a relative thickness $t/c = 12.6\%$. The wing shape is wavy (Fig. 1), with a curved span line, slightly tilted upward (dihedral) at the root and curved downward (anhedral) with drooped tips. Details on the geometry of the IQFoil main wing are given by Macikowski et al. (2023) who investigated several wings with 3D scanning. The wing is placed on a connecting piece specially designed for the experiment (Fig. 3). It allows the wing to be placed just below the support arm that connects it to the force sensor in order to reduce the moment M_y and remain within the range of the sensor. This support arm is the standard carbon mast of the IQFoil windfoil with a wingspan of 1011 mm. The reference frame used is shown in Fig. 3.

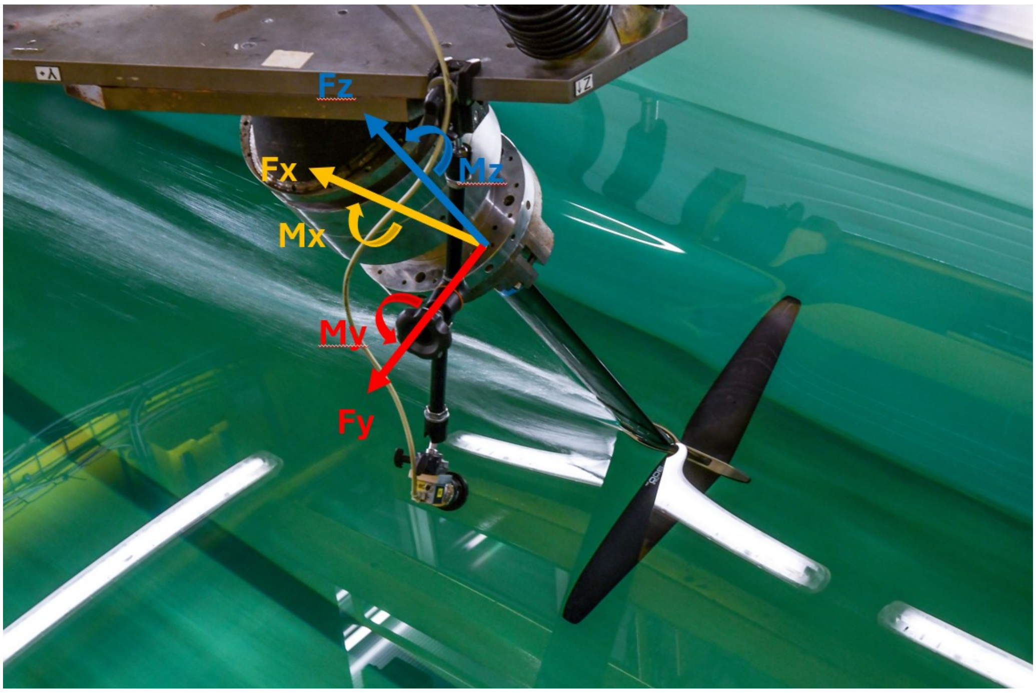

Figure 3. Wing set-up and reference frame.

Special care is taken to align the set-up and calibrate the foil position and angles with a precision level ($\pm 0.05°$) and a laser rangefinder. The zero yaw angle R_z is verified by canceling the lateral force F_y during preliminary runs with zero heel. The overall accuracy is estimated to 2 mm on immersion height and 0.1° on angles. Fifteen minutes are awaited between each run and it is checked that no motion is visible in the tank (note that towing the foil makes far less perturbations in the water than towing a hull model, then motion vanishing is faster than during usual towing tests). It is considered that the tests are performed in quiet water with a turbulence intensity close to zero. The force sensor is zeroed with the foil in the testing position during 5 s at the beginning of each run before starting the carriage. The weight-buoyancy force is then eliminated. The actual run duration at steady speed $U = 7\,\mathrm{m\,s^{-1}}$ is 5 s and the measured forces are averaged on the last 3 s of the steady stage.

For each configuration tested (angle of attack, heel angle, immersion), two tests are carried out. A first one in complete assembly with the wing on the connecting piece (Fig. 3) and a second one with the mast and connecting piece, without wing, for which the wing is replaced by a part to fill the imprint of the wing in the connecting piece to have a smooth shape. All the results presented here are obtained after subtracting the forces measured without the wing (tare test) from the forces measured in the complete assembly, in the same configuration (α, h/c, θ), in order to isolate the contribution of the wing only. The tare forces revealed as follows: lift is insignificant and drag is linear with the immersed shaft length ($C_D^{tare} = 0.0012\,h/c\,\cos\theta + 0.0032$, C_D^{tare} defined with respect to the wing surface area), dominated by the area projected in the onset flow direction. Then, assuming a linear superposition of the contributions, the force coefficients of the wing alone are analyzed by subtracting the tare force coefficients to the coefficients measured with the wing. The interactions are neglected, and this is a clear limitation of the present analysis. The main perturbation comes from the piece connecting the wing to the shaft. Moreover, results at the lowest immersion depth should be considered with caution because the connecting piece emerges and dominates the spray and free surface deformation in the central region. It is hoped that the high aspect ratio of the wing is on our side.

3 RESULTS

All the results presented in this section correspond to the wing alone (after subtracting the tare forces of the mast and the connecting piece measured without the wing). We note:

- h/c, the immersion depth of the foil h, corresponding to the flying height, made dimensionless by the chord c of the wing in the center. h represents the height between the free surface and the center O of the reference frame linked to the wing located at mid-chord of the wing in the symmetry plane of the wing;
- $Fr = U/\sqrt{gc}$, the Froude number related to the chord c of the wing. U corresponds to the speed of the carriage in $\mathrm{m\,s^{-1}}$ ($U = 7\,\mathrm{m\,s^{-1}}$, $Fr = 6.3$ for all results presented here), $g = 9.81\,\mathrm{m\,s^{-2}}$ the acceleration of gravity;
- α, the wing angle of attack expressed in degrees, except in Eq. (1) and in $\mathrm{d}C_L/\mathrm{d}\alpha$ where it is in radians, defined as the angle between the wing chord in the center and the flow direction, in the wing symmetry plane (inclined from the vertical by the heel angle);
- $C_L = L/0.5\rho SU^2$, the lift coefficient, with L the lift force in N perpendicular to the speed U of the carriage in the wing symmetry plane, normal to the span, directed towards the balance, S the lifting surface of the wing and $\rho = 1000\,\mathrm{kg\,m^{-3}}$ the density of the water in the tank;
- $C_D = D/0.5\rho SU^2$, the drag coefficient, with D the drag force in N parallel and opposite to the speed U of the carriage.

Results are shown for a carriage velocity $U = 7\,\mathrm{m\,s^{-1}}$, corresponding to a Froude number $Fr = 6.3$. Heel angles from 0° up to 30° are tested, corresponding to the realistic range in IQFoil sailing. Extra tests are performed at a heel angle of 60°, which is not observed in IQFoil sailing, but is common for kitefoils that use a rather similar foil.

3.1 Variations with Angle of Attack

From visual observation, we note that the wave field is in phase opposition if the foil is in a case of upward lift ($\alpha \geq -2°$) or downward lift ($\alpha \leq -2°$). We can also notice, in the case of the lifting foil, that the amplitude of the free surface reaches its maximum for immersion $h/c = 1.5$. In the case of a downward force, the amplitude of the wave field is greater for low values of immersion depth and tends towards zero when the immersion increases.

Variations of the lift and drag coefficients with the angle of attack for $0°$ heel angle and velocity $U = 7\,\mathrm{m\,s^{-1}}$ are shown on Fig. 4 for different values of the immersion depth. The lift varies linearly with angle of attack in the investigated range, with a slope that slightly decreases when approaching the free surface (see Section 4 for more details). The lift coefficient is lower for a closer proximity to the free surface, particularly for higher incidences, where the surface is the most deformed. For example, for $\alpha = 4°$, C_L decreases by 11% at $h/c = 1$ compared to $h/c = 6$, and by 36% at $h/c = 0.25$. The zero-lift angle is not $0°$ due to the section camber. It is around $-1.7°$, except for a very low immersion depth where it reaches $-0.8°$ at $h/c = 0.25$ (see Section 4 for more details). We can consider that the effective camber is reduced by the close vicinity of the free surface. The variation of the drag coefficient with angle of attack is parabolic, according to the thin wing theory without a free surface. The drag is lower for a lower immersion depth as the lift is decreased, showing that the induced drag associated with lift generation is dominant compared to the additional wave drag. For example, for $\alpha = 4°$, C_D decreases by 10% at $h/c = 1$ compared to $h/c = 6$, and by 25% at $h/c = 0.25$.

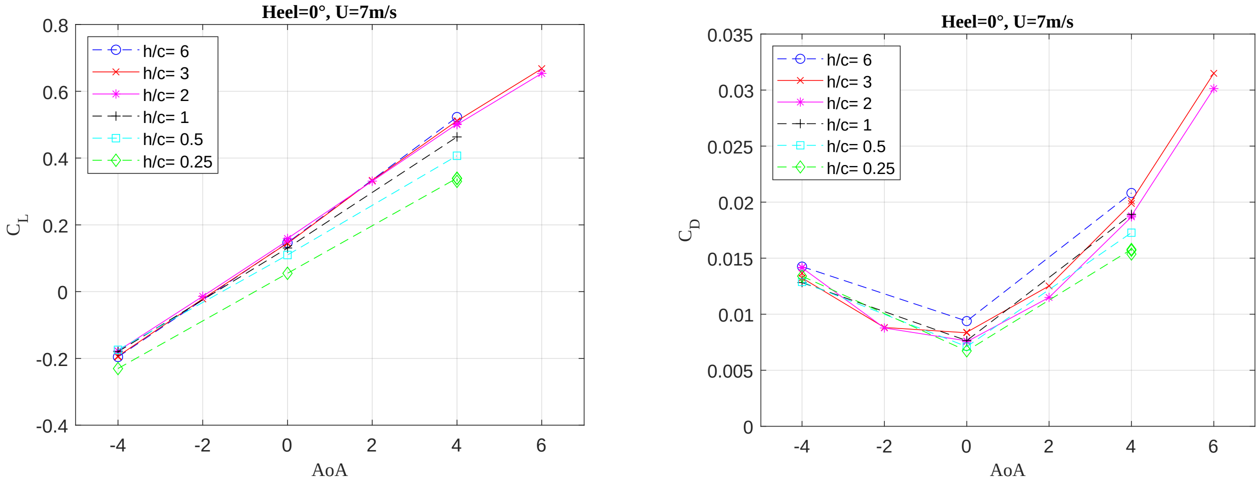

Figure 4. Lift C_L and drag C_D coefficients as a function of angle of attack (AoA) for different values of the immersion depth h/c for heel angle $\theta = 0°$ and velocity $U = 7\,\mathrm{m\,s^{-1}}$.

Figure 5 shows the variations of force coefficients with the angle of attack for different values of the heel angle, at a constant moderate immersion depth $h/c = 2$. Both lift and drag decrease a little for increasing heel angle, as the upper part of the wing gets closer to the surface. At the highest heel angle of $60°$, the upper part of the wing is out of the water and the hydrodynamic forces are more significantly reduced (note that the coefficients C_L and C_D are defined with the full wing surface S).

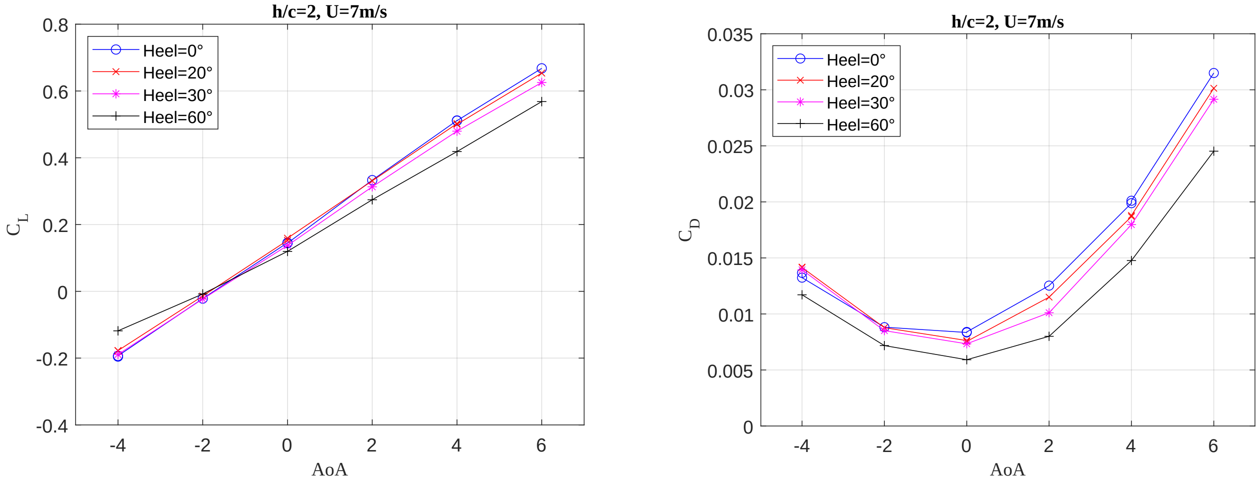

Figure 5. Lift C_L and drag C_D coefficients as a function of angle of attack (AoA) for different values of heel angle θ, at the immersion depth $h/c = 2$ and velocity $U = 7\,\mathrm{m\,s^{-1}}$.

3.2 Variations with Immersion Depth

Figures 6 and 7 show how the force coefficients vary with the immersion depth for different values of the heel angle and the angle of attack. For moderate heel angles, the effect of the free surface disappears for immersion depths h/c higher than 3. For a lower immersion depth (higher flying height), the hydrodynamic forces decrease with the proximity to the free surface, first gently and then more rapidly when the wing starts to emerge. The top part of the wing reaches the free surface at $h/c = 1.09$ for 20° heel angle, $h/c = 1.6$ for 30° heel angle, and $h/c = 2.96$ for 60° heel angle. Sharp drops of the lift are noticeable when the wing is highly loaded (high α) at $h/c = 0.75$ for 20° heel angle, and $h/c = 1 - 1.25$ for 30° heel angle. These are due to the development of ventilation on the upper half of the wing, where an air pocket settles on the suction side and makes the lift drop (see Fig. 8). The lift coefficient recovers for even lower h/c because no ventilation occurs in these cases.

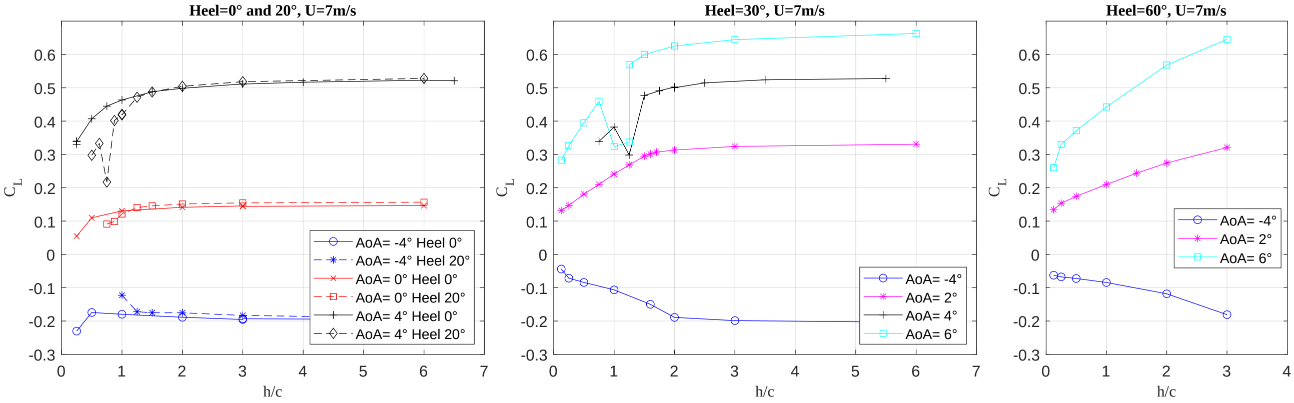

Figure 6. Lift coefficient C_L as a function of immersion depth h/c for different angles of attack α, at the velocity $U = 7\,\mathrm{m\,s^{-1}}$, for different values of heel angle: $\theta = 0°$ and $\theta = 20°$ (left), $\theta = 30°$ (center), $\theta = 60°$ (right).

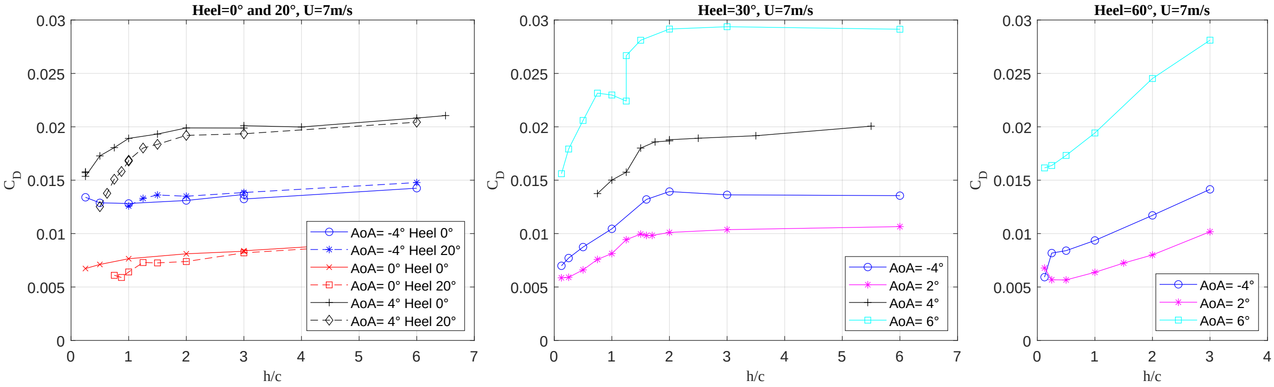

Figure 7. Drag coefficient C_D as a function of immersion depth h/c for different angles of attack α, at the velocity $U = 7\,\mathrm{m\,s^{-1}}$, for different values of heel angle: $\theta = 0°$ and $\theta = 20°$ (left), $\theta = 30°$ (center), $\theta = 60°$ (right).

Interestingly, several cases do not exhibit ventilation even if the wing emerges the static free surface at rest. First, when the angle of the wing span with the surface is too high, as is the case for 60° heel angle, the air is not able to propagate down the steep suction side of the wing. Then, ventilation does not set in and the reduction of lift and drag is smooth and related to the reduction of the submerged lifting surface. Second, in several cases where the wing slightly emerges at rest, once the carriage is up to speed, the deformation of the surface fully submerges the wing. This case is illustrated on Fig. 9. In this case, some ventilation starts developing at the beginning or the run, but it disappears before the end of the acceleration phase, and the constant speed phase where the measurement is made shows a fully wetted wing under the deformed free surface. Then, the lift coefficient in this case ($\theta = 20°$, $h/c = 0.875$, $\alpha = 4°$, $U = 7\,\mathrm{m\,s^{-1}}$) is $C_L = 0.4$, twice as much as the case of slightly lower immersion depth ($h/c = 0.75$) where the ventilation settles and $C_L = 0.2$. This favorable behavior may be the reason for the particular shape of the IQFoil main wing. Indeed, the very much penalizing ventilation phenomenon does not appear just when the wing pierces the surface, but when it emerges significantly, making it more forgiving for the highest flying height. This behavior was not observed with a straight wing (Hauville et al., 2024) (and a future paper from the same authors) and is believed to be an advantage of the drooped tips.

Figure 8. Ventilation on the wing piercing the free surface. (left) Full ventilation for heel angle $\theta = 20°$, $h/c = 0.75$, $\alpha = 6°$, $U = 7\,\mathrm{m\,s^{-1}}$; (right) Partial ventilation for $\theta = 30°$, $h/c = 1.25$, $\alpha = 4°$, $U = 7\,\mathrm{m\,s^{-1}}$.

Figure 9. No ventilation case although the wing pierces the undeformed free surface at rest, for heel angle $\theta = 20°$, $h/c = 0.875$, $\alpha = 4°$, $U = 7\,\mathrm{m\,s^{-1}}$. Top left: front view at rest; top right: top view at speed; bottom left: front view at speed; bottom right: rear view at speed.

4 ANALYSIS

The following section aims at a global characterization of the hydrodynamic forces variations with the different parameters, in the perspective to build a global force model taking into account the surface proximity. The particular cases affected by ventilation are not addressed here and would need more work. The results presented in section 3 show that in the studied parameter range, the lift coefficient C_L is a linear function of the angle of attack (Fig. 4 and 5), and the drag coefficient C_D is a second-order polynomial function of the angle of attack, then a second-order polynomial function of the lift coefficient too.

One can then write:

$$C_L = \frac{d\,C_L}{d\,\alpha}(\alpha - \alpha_0), \tag{1}$$

$$C_D = C_{D_{min}} + \frac{(C_L - C_{L_{md}})^2}{\pi\, A_{Reff}} \quad ; \quad A_{Reff} = e\, A_R. \tag{2}$$

The method developed by Traub (2022) allows for describing the force coefficients as functions of angle of attack for each value of the heel angle and immersion depth with the following parameters: the lift coefficient slope $d\,C_L/d\,\alpha$ and the zero-lift angle α_0 are determined by a linear fit of $C_L(\alpha)$; the minimum drag coefficient $C_{D_{min}}$, the lift coefficient at minimum drag $C_{L_{md}}$, and the effective aspect ratio A_{Reff}, or equivalently the Oswald coefficient e, are determined by a quadratic fit of $C_D(C_L)$. We obtain:

$$C_D \approx B_1 C_L^2 + B_2 C_L + B_3, \tag{3}$$

which yields:

$$C_{L_{md}} = \frac{B_2}{-2\,B_1} \quad ; \quad C_{D_{min}} = B_3 - \frac{B_2^2}{4\,B_1} \quad ; \quad A_{Reff} = \frac{1}{\pi\,B_1} = e\,A_R. \tag{4}$$

Figure 10 shows the variations of the lift coefficient slope $d\,C_L/d\,\alpha$ and the zero-lift angle α_0 as a function of immersion depth h/c, for different heel angles. The slope $d\,C_L/d\,\alpha$ equals the theoretical slope $2\pi A_R/2 + \sqrt{A_R^2 + 4}$ for the deeply immersed wing at low heel angle, and reduces when approaching the free surface, first slightly, then rapidly, particularly when the heeled wing emerges and the immersed lifting surface is reduced (note that force coefficients are defined with respect to the full wing projected area). The zero-lift angle α_0 is almost constant ($\alpha_0 = -1.9^\circ \pm 0.2^\circ$), and does not depend much on immersion nor heel for $h/c > 1$. For lower immersion depths, α_0 increases at zero or low heel angle (maximum $\alpha_0 \approx -0.75$ at $h/c = 0.125$, but seems to decrease a little for the highest heel angles.

Variations of the minimum drag coefficient $C_{D_{min}}$, the lift coefficient at minimum drag $C_{L_{md}}$ and the Oswald coefficient e as a function of immersion depth h/c for different heel angles are shown on Figure 11. Note that for heel angles $\theta = 30^\circ$ and $\theta = 60^\circ$, the regression coefficient of the $C_D(C_L)$ quadratic fit is rather low; then the values of these three coefficients are not well defined and these two highest heel angles are not considered in the comments below. The general trend of the minimum drag for low heel angles is a slight decrease when approaching the free surface, from $C_{D_{min}} = (9.1 \pm 0.1)10^{-3}$ at $h/c = 6$, down to $C_{D_{min}} = (7.2 \pm 0.2)10^{-3}$ at $h/c = 1$. The lift coefficient at minimum drag does not vary significantly with immersion depth nor heel angle and is given by $C_{L_{md}} = (0.1 \pm 0.02)$. The trend of the Oswald coefficient is very similar to the trend observed for the lift slope, but it is noticeable that the value is rather low (e from 0.5 at $h/c = 6$, down to 0.32 at $h/c = 0.125$). This suggests that the spanwise distribution of circulation is far from an elliptic profile, known to be optimal in terms of induced drag with $e = 1$. This may be the sign that the IQFoil wing is more optimized in terms of viscous drag than in terms of induced drag.

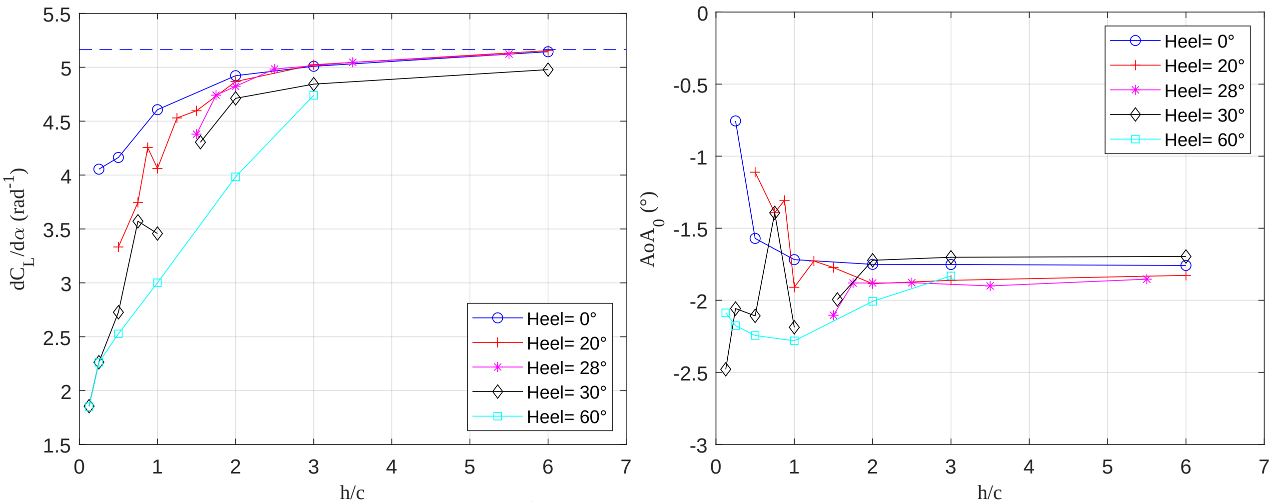

Figure 10. Lift coefficient slope $dC_L/d\alpha$ (left) and zero-lift angle α_0 (right) as a function of immersion depth h/c for different heel angles and $U = 7\,\mathrm{m\,s^{-1}}$. The theoretical slope of $dC_L/d\alpha = 2\pi A_R/2 + \sqrt{A_R^2 + 4}$ is shown with a dashed line for reference.

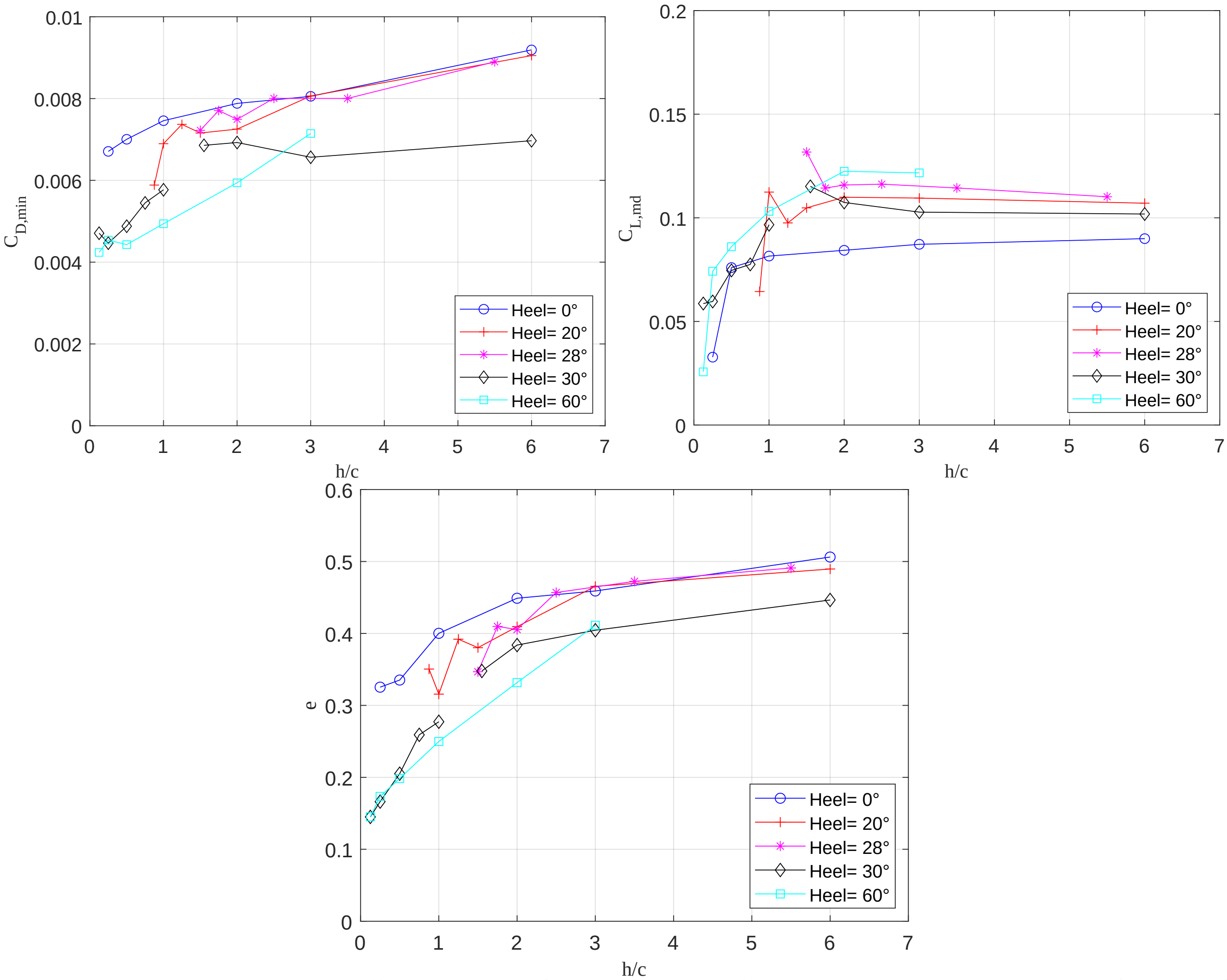

Figure 11. Minimum drag coefficient $C_{D_{min}}$ (top left), lift coefficient at minimum drag $C_{L_{md}}$ (top right) and Oswald coefficient e (bottom) as a function of immersion depth h/c for different heel angles and $U = 7\,\mathrm{m\,s^{-1}}$.

5 CONCLUSIONS

A towing tank test campaign was presented where the main lifting foil of the Olympic class windfoil (IQ-Foil) was tested in the Centrale Nantes towing tank, at high chord-based Froude number ($Fr = 6.3$). The lift and drag coefficients were determined for varying immersion depth-to-chord ratio h/c, heel angle θ and angle of attack α. The results show that the lift coefficient of the horizontal wing ($\theta = 0°$) varies linearly with the angle of attack, with a slope that slightly decreases as the wing approaches the free surface. The zero-lift angle due to the section camber ($\alpha_0 = -1.7° \pm 0.2°$) does not vary with the immersion depth, except very close to the free surface, where it is increased up to $\alpha_0 = -0.75°$ for $h/c = 0.125$. The drag coefficient variation with angle of attack is parabolic. Both lift and drag decrease monotonically when approaching the free surface (higher flying height), but the effect of the surface becomes negligible for a depth-to-chord ratio h/c higher than 3. These observations remain valid for a moderate heel angle (up to 30°), as long as the wing remains below the surface. When the heeled wing slightly emerges from the non-deformed free surface (at rest), the surface deformation (at speed) may be such that the wing becomes fully wetted and the lift is only weakly affected. This behavior is probably favored by the particular shape of the wing which is curved along the span. When the wing emerges a little more and is heavily loaded (high α), ventilation may occur with an air pocket sucked along the upper side of the wing, causing a sharp drop of the lift. These original experimental results provide a useful benchmark data basis for the validation of numerical simulations and may be used to build a surrogate hydrodynamic force model to be used in a Velocity Prediction Program (VPP). The moment results will be analyzed in a future work, to provide the centers of pressure. The presented results are measured on a full-scale IQFoil wing at a velocity $U = 7\,\mathrm{m\,s^{-1}}$ which is less than the common real sailing speed. The full-scale Reynolds and Froude numbers are then a little bit higher. Finally, it should be kept in mind that these results are obtained in the flow conditions of a towing tank, which may differ from the real sailing conditions in terms of turbulence, waves, motion, etc. In terms of ventilation in particular, it has been observed that ventilation inception and desinence in the laboratory differ significantly from real-life conditions (Augier et al., 2024). Moreover, interactions between the different parts of the foil package are not considered here.

ACKNOWLEDGEMENTS

This work was funded by the *Agence Nationale de La Recherche* (ANR) through grant n°ANR-19-STHP-0002. The authors warmly thank Bertrand Malas and Anne Levesque for their help in the tank testing, and Arnaud Merrien and all the technical staff from Ecole Navale for the design and realization of the experimental setup.

REFERENCES

Augier, B., Hochhausen, M., Iachkine, P., Sahores, R., Clouet, Y., Fermigier, M., and Clanet, C. (2024). Test and control of ventilation on Kitefoil shaft. *Sports Physics*. Rennes, France.

Binns, J., Brandner, P., and Plouhinec, J. (2008). The effect of heel angle and free-surface proximity on the performance and strut wake of a moth sailing dinghy rudder T-foil. *3rd High Performance Yacht Design Conference, Auckland*.

Daskovsky, M. (2000). The hydrofoil in surface proximity, theory and experiment. *Ocean Engineering* 27.10, pp. 1129–1159.

de la Hougue, A., Androuin, G., Pernod, L., Sacher, M., Augier, B., Bot, P., and Iachkine, P. (2022). Influence of shaft stiffness on the performance of a plane-like hydrofoil. *25e Congrès Français de Mécanique*. Nantes, France.

de la Hougue, A., Augier, B., Iachkine, P., Le Vergos, P., Sacher, M., and Bot, P. (2021). Geometric discrepancies in Olympic windsurf foils: measurements versus athletes' feedback. *Sports Physics 2021*. Lyon, France.

Drela, M. and Youngren, H. (2011). *Athena Vortex Lattice (AVL)*. Massachusetts Inst. of Technology, Cambridge, MA.

Faltinsen, O. (2005). Hydrodynamics of high-speed marine vehicles. *Cambridge University Press google schola* 3, pp. 386–391.

Harwood, C., Felli, M., Falchi, M., Ceccio, S., and Young, Y. (2019). The hydroelastic response of a surface-piercing hydrofoil in multi-phase flows. Part 1. Passive hydroelasticity. *Journal of Fluid Mechanics* 881, pp. 313–364. DOI: `https://doi.org/10.1017/jfm.2019.691`.

Harwood, C., Felli, M., Falchi, M., Garg, N., Ceccio, S., and Young, Y. (2020). The hydroelastic response of a surface-piercing hydrofoil in multiphase flows. Part 2. Modal parameters and generalized fluid forces. *Journal of Fluid Mechanics* 884, A3. DOI: `https://doi.org/10.1017/jfm.2019.871`.

Harwood, C., Young, Y., and Ceccio, S. (2016). Ventilated cavities on a surface-piercing hydrofoil at moderate Froude numbers: Cavity formation, elimination and stability. *Journal of Fluid Mechanics* 800. DOI: `https://doi.org/10.1017/jfm.2016.373`.

Hauville, F., Bot, P., Ploé, P., Malas, B., Merrien, A., and Levesque, A. (2024). Essai en Bassin de Traction d'un Hydrofoil en Proximité Immédiate de la Surface Libre. *19eme Journées de l'Hydrodynamique*. Nantes, France.

Hochhausen, M., Sacher, M., Augier, B., Nicolas, H., Bot, P., Hauville, F., and Clouet, Y. (2024). How sailor morphology affects Olympic windfoil performance? *Sports Physics 2024*. Rennes, France.

Hou, J., Liu, G., Tan, Q., Mok, K., Song, W., Chan, K., So, R.-H., Zhou, P., and Zhang, X. (2024a). Velocity prediction program for windsurfing: A hierarchical approach integrating biomechanical insights. *Ocean Engineering* 312, p. 119070. DOI: `https://doi.org/10.1016/j.oceaneng.2024.119070`.

Hou, J., Mok, K., Cantos, S., Bertin, C., Chan, K., Zhou, P., Zhong, S., and Zhang, X. (2024b). Numerical simulation of windsurfing sail aerodynamics: Insights into forces and flow characteristics. *Ocean Engineering* 300, p. 117477. DOI: `https://doi.org/10.1016/j.oceaneng.2024.117477`.

Hough, G. and Moran, J. (1969). Froude number effects on two-dimensional hydrofoils. *Journal of Ship Research* 13.01, pp. 53–60.

Jego, C. (2022). CFD investigation of the impact of the free surface proximity on the performances of a T-shaped Olympic Class Kitefoil hydrofoil. MSc. Thesis. University of Southampton.

Macikowski, Z., Karczewski, A., and Krata, P. (2023). Influence of deviation of section angle of attack in serially produced hydrofoils on the lift-drag characteristics. *X International Conference on Computational Methods in Marine Engineering MARINE 2023*. Madrid, Spain.

Mok, K., Zhou, P., Hou, J., Zhong, S., Zhang, X., So, R.-H., and Chan, K. (2023). Performance of a windsurfing sail under steady condition. *Ocean Engineering* 289. DOI: `https://doi.org/10.1016/j.oceaneng.2023.116295`.

Nicolas, H., Perali, P., Sacher, M., and Bot, P. (2023). Boundary element method analysis of 3d effects and free-surface proximity on hydrofoil lift and drag coefficients in varied operating conditions. *Journal of Sailing Technology* 8.01, pp. 183–199.

Parkin, B., Perry, B., and Wu, T. (1955). *Pressure Distribution on a Hydrofoil Running near the Water Surface*. 47-2. American Institute of Physics.

Perali, P., Sacher, M., Leroux, J.-B., Wackers, J., Augier, B., Hauville, F., and Bot, P. (2022). Comparaison de Conditions de Surface Libre Linéarisées Pour l'étude d'un Hydrofoil Submergé à l'aide d'une Approche Potentielle. *25ème Congrès Français de Mécanique*.

Perali, P., Sacher, M., Leroux, J.-B., Wackers, J., Augier, B., Hauville, F., and Bot, P. (2024). Performance prediction of a hydrofoil near the free surface using low (BEM) and high (RANS) fidelity methods. *Applied Ocean Research* 151, p. 104157. DOI: `https://doi.org/10.1016/j.apor.2024.104157`.

Pernod, L., Sacher, M., Wackers, J., Augier, B., and Bot, P. (2023). Free-surface effects on two-dimensional hydrofoils by RANS-VOF simulations. *Journal of Sailing Technology* 8.01, pp. 24–38.

Traub, L. (2022). Calculation of the Oswald Efficiency Factor from Drag Polars: A Critical Assessment. *Journal of Aircraft* 59.6, pp. 1608–1615.

Wadlin, K. and Christopher, K. (1958). *A Method for Calculation of Hydrodynamic Lift for Submerged and Planing Rectangular Lifting Surfaces*. Technical report 4168. Langley Field, Va.: National Advisory Committee for Aeronautics.

Wadlin, K., Shuford Jr., C., and McGehee, J. (1955). *A Theoretical and Experimental Investigation of the Lift and Drag Characteristics of Hydrofoils at Subcritical and Supercritical Speeds*. Technical report 1232. Langley Field, Va.: National Advisory Committee for Aeronautics.